



Research Article

Study of Microstructure and Properties of 316L with Selective Laser Melting Based on Multivariate Interaction Influence

Jianfeng Sun ¹, Lu Shen,² Weiqiang Wang,¹ Zhu Liu,³ Huaming Chen,¹ and Jieli Duan ⁴

¹College of Engineering, South China Agricultural University, Guangzhou 510642, China

²Medical Equipment Department, The Fifth Affiliated Hospital of Guangzhou Medical University, Guangzhou 510700, China

³School of Materials, The University of Manchester, Manchester M139PL, UK

⁴Engineering Fundamental Teaching and Training Center, South China Agricultural University, Guangzhou 510642, China

Correspondence should be addressed to Jieli Duan; duanjieli@scau.edu.cn

Received 5 June 2019; Revised 20 September 2019; Accepted 3 October 2019; Published 20 January 2020

Academic Editor: Fulvio Lavecchia

Copyright © 2020 Jianfeng Sun et al. This is an open access article distributed under the Creative Commons Attribution License, which permits unrestricted use, distribution, and reproduction in any medium, provided the original work is properly cited.

The selective laser melting technique is widely used in aerospace and biomedical industries, and the performance of formed 316L parts is significantly subject to the forming angle. As the selective laser melting 316L parts are constrained by multiple performance indexes, the study involves multivariate interaction influenced on the forming parameters such as the angle with the xz plane, the angle with the xy plane, laser power, scan speed, powder thickness, and hatching space on the indexes like tensile strength, density, and surface roughness with linear regression equations based on multiobjective optimization to obtain the best process parameters. The study results of microstructure performance of the formed 316L parts show that the angle with the xz plane has significant effect on the experiment indexes, while the layer thickness has the greatest effect on the indexes. After stretching, the molten pools are obviously elongated and the microstructure of the formed 316L parts is composed of equiaxed crystals and columnar crystals with a grain width of 0.28–0.4 μm . The secondary growth of the dendrites is not obvious, and the crystallinity of the selective laser melting 316L parts is not as good as the standard parts, with the microstructure showing directional solidification due to grain refinement and microscopic distortion of crystals. As the fracture has dimples, it is a ductile fracture and typical plastic fracture. The hardness near the fracture is higher than that of the substrate, whilst the indexes regarding the selective laser melting parts are higher than the ASTM-A182 and ASTM-F3184-16 standards. Since the theoretical model built in this study has less error, the findings have practical engineering application value.

1. Introduction

The selective laser melting technique is a newly developed powder bed fusion additive manufacturing technique. The principle is that the metal powder is fused by laser and solidified to form a molten pool, and then multistacked by layer to produce a three-dimensional part [1]. As for a small number of customized parts, the technique has several advantages, such as short time consumption, fast response, and high efficiency [2]. In recent years, additive manufacturing has made great breakthroughs in various industries, especially in aerospace and biomedical fields [3, 4], showing broad application prospects.

The selective laser melting process parameters have a great effect on the mechanical properties, surface quality, and friction performance of the formed parts. Some studies have shown that the laser power and scan speed have the most significant effect on the density of the sample [2, 5–8], and the scan speed, layer thickness, and manufacturing direction have a certain effect on the surface roughness and dimensional accuracy of the formed parts [9]. The lower the laser power, the lower the density and hardness of the sample, and the less the fusion at the boundary of the molten pool [10]. When the forming direction is inclined from 45° to 90°, the strength and fatigue resistance decrease and the elongation at break increases by more than 50% [11]. Wang

et al. [12] studied the effect of the selective laser melting scanning strategy on residual stress and surface quality of the formed parts. The results show that the 316L stainless steel parts can achieve 99.37% of density with the scanning strategy of helical segmentation to effectively control the residual stress of the SLM 316L stainless steel parts. Dilip et al. [13] studied the effect of heat treatment on the microstructure and properties of the SLM HY100 steel. The results show that the microstructure of the parts after heat treatment is finer and more uniform with the mechanical properties being improved. Amato et al. [14] of the University of Tennessee in the United States studied the SLM Inconel 718 cylindrical parts. The results show that the Vickers hardness of untreated, HIP-treated, and heat-treated parts is 3.9 GPa, 5.7 GPa, and 4.6 GPa, respectively. Wei et al. [15] studied the microstructure and properties of stainless steel nanohydroxyapatite medical composites with selective laser melting technique. The results show that the tensile strength, elastic modulus, and hardness of the SS/NHA prototype obtained under the optimum process conditions are higher than the human bone, which provides the possibility to prepare the SS/NHA porous scaffold with AP mechanical properties of the weight-bearing bone.

Selective laser melting direction is one of the important factors affecting the performance of the formed parts [16, 17]. At present, most of the forming parameters are obtained without considering the forming direction (the angle with the xy plane is default as 90°), but practically, the changes in the angle with the xy plane and the angle with the xz plane bring significant variation of density, surface roughness (step effect), and mechanical properties of the formed parts [18–20]. In the laser forming process, the thermal gradient and the cooling rate of the formed part change with the forming angle and a complex dynamic fluid flow is generated in the molten pool. These complex phenomena affect crystal growth and orientation [21], resulting in material sputtering and microstructure defects, mainly manifested by micropores, high residual stress, and large surface roughness [12, 22, 23]. These defects cause premature failure under fatigue loading. At present, there are many studies on the forming parameters of the 316L stainless steel with selective laser melting, mainly focusing on the effect of the single factor on the performance of the single formed part [24, 25], rather than the effect of multifactors on multiple indexes. The study on the interaction effect of multiple forming directions on the density, surface roughness, and tensile strength of the formed parts has not been reported [26].

In this study, tensile parts with various forming angles were prepared by selective laser melting for the test of density, surface roughness, and mechanical properties of the parts, analysis of microstructure and fracture morphology of the parts with various forming angles, and exploration of the microstructure properties and forming mechanism in different areas and the effect on tensile mechanical properties, providing a theoretical basis for the control of microstructure and mechanical properties of the selective laser melting parts.

2. Experimental Materials and Methods

2.1. Experimental Equipment and Materials. In the experiment, the following products of Guangzhou Riton Laser Co., Ltd. were selected: the D280 AM machine with an accuracy of ± 0.02 mm, laser wavelength of $1.064 \mu\text{m}$, focused spot diameter of $20\text{--}80 \mu\text{m}$, and layer thickness of $20\text{--}80 \mu\text{m}$ for forming parts; WD-E stretching tester with a pressure sensor of $0\text{--}20$ kN for the tensile test; KERN analytical balance ABJ 320-4NM with a range of 320 g and accuracy of 0.0001 g for quality measurement; TIME3220T roughness meter with a measurement platform size of $400 \text{ mm} \times 250 \text{ mm} \times 70 \text{ mm}$, lift height of 300 ± 1 mm, x -direction fine tune of ± 12.5 mm, y -direction fine tune of ± 12.5 mm, rotating coarse tune of 360° , and fine tune of $\pm 5^\circ$ for detecting surface roughness; MQX1200-40 atmosphere box furnace with a maximum temperature of 1200° and temperature control accuracy of $\pm 1^\circ$ for heat treatment; XQ-1 metallographic specimen mounting press and YMPZ-1 automatic metallographic specimen grinding and polishing machine for metallographic preparation; EVO18 ZEISS scanning electron microscope with a magnification of $5\text{--}1,000,000\times$ and acceleration voltage of $0.2\text{--}30$ kV for microstructure observation; and SmartLab (9) X-ray diffractometer (XRD) with an X-ray generator of fine focusing 9 kW knob, X-ray generator filament of $0.4 \text{ mm} \times 8 \text{ mm}$, and goniometer minimum step size of $1/10000^\circ$ for phase analysis.

316L stainless steel powder (MTI S01C) is selected from Guangzhou Material Technology Innovation Co., Ltd. with the chemical composition parameters shown in Table 1, and the microstructure of powder is shown in Figure 1. The powder diameter is D10: $23.48 \mu\text{m}$, D50: $31.13 \mu\text{m}$, and D90: $42.26 \mu\text{m}$.

2.2. Experimental Design. The response surface method is to study the influence of multiple factors on indicators based on both mathematics and statistics. The least square method is used to obtain the regression equation by second-order polynomial fitting, and the most suitable model is selected according to the significance test. The true functional relationship between the response Y and the independent variables $\xi_1, \xi_2, \dots, \xi_k$ in the response surface method can be expressed as

$$Y = f(\xi_1, \xi_2, \dots, \xi_k) + \varepsilon, \quad (1)$$

where f is unknown, ξ is another variable not included in f , and ε is the error term.

For second-order response surfaces, the following polynomial is used:

$$Y = b_0 + \sum_{i=1}^k b_i x_i + \sum b_{ii} x_{ii}^2 + \sum_i \sum_j b_{ij} x_i x_j + \varepsilon, \quad i \leq j, \quad (2)$$

where b_0 is the intercept, b_i , b_{ii} , and b_{ij} are the regression coefficients, and x_i , x_{ii} , and x_{ij} are the horizontally encoding variables.

TABLE 1: Chemical composition table of 316L stainless steel powder.

Composition (wt.%)	C	Cr	Fe	Mn	Mo	Ni	Si	P	N	S
	0.01%	17.66%	Bal.	0.05%	2.40%	12.86%	0.74%	—	0.06%	0.0007%

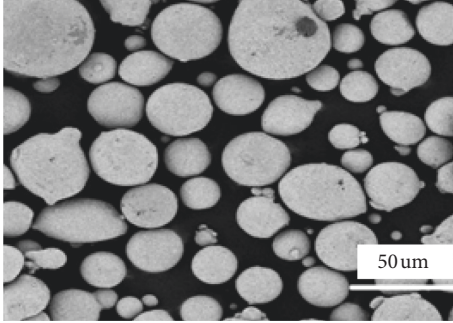


FIGURE 1: Powder of 316L.

The experimental design model of response surface method mainly includes central composite test design, BOX design, and secondary saturated D-optimal design. This study involves six factors and three levels in the BOX for experimental design.

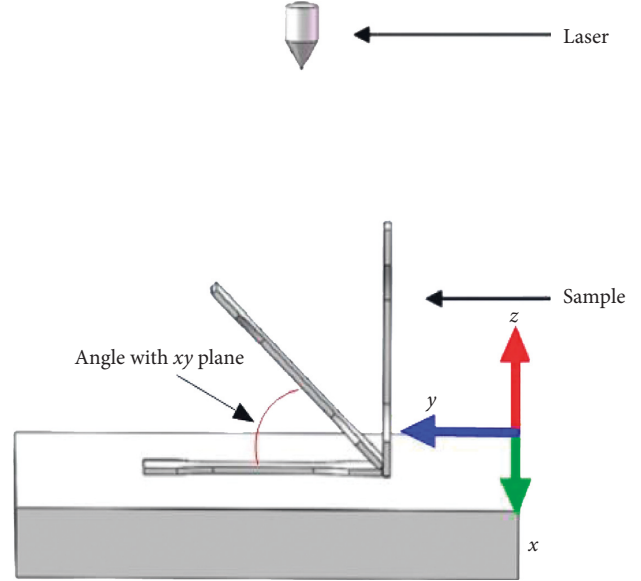
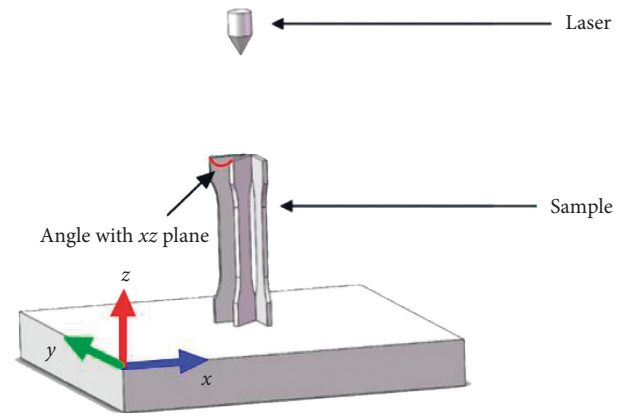
The response surface method was used to optimize the process parameters of 316L stainless steel with selective laser melting. The laser power A , scan speed B , hatching space C , layer thickness D , the angle with the xy plane F (shown in Figure 2), and the angle with the xz plane E (shown in Figure 3) were selected. The horizontal values of each factor are shown in Table 2. The tensile specimen specifications are calculated according to ISO 6892-1: 2009, ASTM E8/8M. In this study, 316L stainless steel samples were formed with D280 (shown in Figure 4), the density of the sample Y_2 was measured by the Archimedes drainage method, the surface roughness of the sample Y_1 was measured with the roughness meter, and the tensile limit Y_3 and the elongation rate Y_4 were measured on the tensile test bench. The Archimedes principle formulas are as follows:

$$\rho_2 = \frac{m_1}{(m_3/\rho_1) - ((m_2 - m_1)/\rho_0)} \quad (3)$$

$$\text{then } \rho = \rho_2/\rho_3,$$

where m_1 is the mass (g) of the formed part in the air before sealing wax; m_2 is the mass (g) of the formed part in the air after sealing wax; m_3 is the mass (g) of the formed part in the water after sealing wax; ρ is the density (%) of the sample; ρ_0 is the density of the wax, which is 0.880 g/cm^3 ; ρ_1 is the density of the distilled water, which is 1 g/cm^3 ; ρ_2 is the density (g/cm^3) of the formed part; and ρ_3 is the theoretical density of 316L stainless steel material, which is 7.98 g/cm^3 ;

To ensure the adaptability and accuracy of the model, it is necessary to evaluate the predictability. The coefficient of determination R^2 and the adjusted coefficient of determination R^2_{adj} are often used to evaluate the approximation of the regression model [27]. The predicted coefficient of

FIGURE 2: Angle with the xy plane.FIGURE 3: Angle with the xz plane.

determination R^2_{prep} is adopted to evaluate the predictability of the regression model with the following formula:

$$R^2 = \frac{S_{\text{SR}}}{S_{\text{ST}}} = \frac{S_{\text{SR}} - S_{\text{SE}}}{S_{\text{ST}}} = 1 - \frac{\sum_{i=1}^n (\hat{y}_i - y_i)^2}{\sum_{i=1}^n (y_i - \bar{y})^2} \quad (4)$$

where S_{ST} is the sum of squares; S_{SR} is the sum of squared regression; S_{SE} is the sum of squared residuals; \hat{y}_i is the predicted value of the response surface; y_i is the true value of the response at the i^{th} observation; \bar{y} is the mean of the response; and n is the number of alignment runs or observations designed for the experiment. R^2 is a fully fitted metric value, usually requiring a value above 0.9.

TABLE 2: Factor coding and experimental level.

Code	A (W)	B (mm/s)	C (mm)	D (mm)	E (°)	F (°)
1	160	900	0.09	0.04	90	90
0	150	800	0.08	0.03	45	45
-1	140	700	0.07	0.02	0	0



FIGURE 4: Physical image of the tensile specimen after heat treatment.

Adjusted coefficient of determination R_{adj}^2 is obtained by

$$R_{\text{adj}}^2 = 1 - \frac{S_{\text{SE}}/(n-p)}{S_{\text{ST}}/(n-1)} = 1 - \frac{(n-1)}{(n-p)}(1-R^2), \quad (5)$$

where p is the number of regression coefficients in the model and R_{adj}^2 refers to the degree of correlation between all independent variables and dependent variables.

Adjusted coefficient of determination R_{prep}^2 is obtained by

$$R_{\text{pred}}^2 = 1 - \frac{V}{S_{\text{ST}}} = 1 - \frac{\sum_{i=1}^n (\hat{y}_i - y_i)^2}{\sum_{i=1}^n (y_i - \bar{y})^2}, \quad (6)$$

where V is the sum of the squares of the predicted errors; \hat{y}_i is the predicted value of the response at the i^{th} time; and R_{prep}^2 represents the predictability based on the original regression model fitted to the data. In general, for a model with acceptable accuracy, the values of R_{prep}^2 and R^2 should be less than or equal to 0.3.

3. Experimental Results and Discussion

3.1. Analysis of Response Surface Method. Experimental analysis was performed using Design-Expert. The experimental results are shown in Table 3.

3.1.1. Analysis of Variance. The data in Table 3 were treated using multivariate regression fitting to obtain the regression equations of the response surface roughness Y_1 , density Y_2 , tensile strength Y_3 , and elongation Y_4 , respectively, expressed by the laser power A , scan speed B , hatching space C , layer thickness D , the angle with the xz plane E , and the angle with xy plane F :

$$\begin{aligned} Y_1 &= 10.1 + 6.93 \times 10^{-3} B + 2.23 D - 5.65 F - 3.38 DF \\ &\quad - 1.67 A^2 + 1.33 F^2, \\ Y_2 &= 83.92 - 1.791 B - 3.44 C - 5.07 D + 2.84 F - 3.94 AC \\ &\quad - 3.08 B D - 2.25 C D + 2.659 E F - 3.458 C^2, \\ Y_3 &= 193.53 + 5.859 A - 42.997 B - 158.41 D - 45.65 F \\ &\quad + 40.27 A D + 52.73 B D + 84.72 A^2 + 74.16 D^2 + 156.42 F^2, \\ Y_4 &= 4.65 + 3.82 A - 2.39 B - 14.2 D - 6.459 AB + 6.481 AE \\ &\quad - 4.94 B D - 6.38 DF + 4.726 A^2 + 13.57 D^2 + 6.605 F^2. \end{aligned} \quad (7)$$

The response value and variance analysis are shown in Tables 4–7. The p values of the four models are all less than 0.01, indicating that the selected factors in the equations are extremely significant, and p values of lack of fit are all greater than 0.05, which is not significant. For the surface roughness of the sample, the coefficient of determination R^2 is 0.9158, the adjusted coefficient of determination R_{adj}^2 is 0.8283, and the predicted coefficient of determination R_{prep}^2 is 0.5898, representing a difference of 0.326 between the coefficient of determination R^2 and the predicted coefficient of determination R_{prep}^2 . For the density of the sample, the coefficient of determination R^2 is 0.8961, the adjusted coefficient of determination R_{adj}^2 is 0.7881, and the predicted coefficient of determination R_{prep}^2 is 0.5716, representing a difference of 0.3245 between the coefficient of determination R^2 and the predicted coefficient of determination R_{prep}^2 . For the tensile strength, the coefficient of determination R^2 is 0.937, the adjusted coefficient of determination R_{adj}^2 is 0.8715, and the predicted coefficient of determination R_{prep}^2 is 0.6842, representing a difference of 0.2528 between the coefficient of determination R^2 and the predicted coefficient of determination R_{prep}^2 . For the elongation of the sample, the coefficient of determination R^2 is 0.9359, the adjusted coefficient of determination R_{adj}^2 is 0.8693, and the predicted coefficient of determination R_{prep}^2 is 0.679, representing a difference of 0.2569 between the coefficient of determination R^2 and the predicted coefficient of determination R_{prep}^2 . All the above indicates that the response surfaces of the four models have good predictability for the experimental results.

The relationships between the actual values of surface roughness, density, tensile strength, and elongation and the predicted values of the regression models are shown in

TABLE 3: Experimental results.

Exp. no.	Laser power (W)	Scanning speed (mm/s)	Scanning interval (mm)	Layer thickness (mm)	Angle with the xz plane	Angle with the xy plane	Surface roughness (μm)	Relative density (%)	Tensile strength (MPa)	Elongation rate (%)
1	140	700	0.08	0.02	45	45	4.69	87.92	543.69	23.22
2	160	700	0.08	0.02	45	45	6.46	89.59	497.90	45.00
3	140	900	0.08	0.02	45	45	4.62	96.28	507.16	38.40
4	160	900	0.08	0.02	45	45	6.99	89.19	590.96	37.62
5	140	700	0.08	0.04	45	45	8.30	86.31	171.31	2.69
6	160	700	0.08	0.04	45	45	8.87	86.25	449.16	33.63
7	140	900	0.08	0.04	45	45	8.43	75.80	52.87	1.39
8	160	900	0.08	0.04	45	45	11.25	80.07	202.25	3.21
9	150	700	0.07	0.03	0	45	13.43	85.95	313.03	6.18
10	150	900	0.07	0.03	0	45	9.53	82.10	129.84	3.11
11	150	700	0.09	0.03	0	45	9.07	82.17	211.51	3.76
12	150	900	0.09	0.03	0	45	12.44	73.83	138.42	4.42
13	150	700	0.07	0.03	90	45	11.29	86.09	217.35	3.87
14	150	900	0.07	0.03	90	45	12.06	85.89	169.67	5.71
15	150	700	0.09	0.03	90	45	13.50	82.67	116.81	3.79
16	150	900	0.09	0.03	90	45	11.00	73.41	103.16	1.12
17	150	800	0.07	0.02	45	0	10.42	89.49	553.97	29.83
18	150	800	0.09	0.02	45	0	9.72	86.52	536.03	29.28
19	150	800	0.07	0.04	45	0	25.53	73.78	340.04	16.54
20	150	800	0.09	0.04	45	0	18.02	66.18	293.15	9.73
21	150	800	0.07	0.02	45	90	6.45	88.29	457.36	48.52
22	150	800	0.09	0.02	45	90	7.90	92.08	484.48	46.72
23	150	800	0.07	0.04	45	90	5.04	89.11	233.40	6.24
24	150	800	0.09	0.04	45	90	5.64	79.47	221.49	5.11
25	140	800	0.08	0.02	0	45	7.16	90.17	546.57	51.08
26	160	800	0.08	0.02	0	45	6.03	82.10	565.66	33.21
27	140	800	0.08	0.04	0	45	12.21	83.16	72.06	2.33
28	160	800	0.08	0.04	0	45	11.51	87.64	179.40	6.48
29	140	800	0.08	0.02	90	45	5.86	93.39	540.82	23.34
30	160	800	0.08	0.02	90	45	5.97	95.04	517.92	45.01
31	140	800	0.08	0.04	90	45	11.02	73.50	90.66	2.87
32	160	800	0.08	0.04	90	45	10.03	77.03	234.72	19.33
33	150	700	0.08	0.03	0	0	20.17	90.18	419.23	19.90
34	150	900	0.08	0.03	0	0	23.38	86.38	237.74	1.67
35	150	700	0.08	0.03	90	0	17.70	79.39	550.22	16.28
36	150	900	0.08	0.03	90	0	15.21	80.95	404.71	16.19
37	150	700	0.08	0.03	0	90	5.66	90.36	365.37	13.68
38	150	900	0.08	0.03	0	90	5.38	82.70	292.86	4.97
39	150	700	0.08	0.03	90	90	4.36	90.41	330.01	11.12
40	150	900	0.08	0.03	90	90	5.38	87.71	324.01	7.74
41	140	800	0.07	0.03	45	0	16.60	79.59	421.77	21.52
42	160	800	0.07	0.03	45	0	11.52	87.11	536.21	26.19
43	140	800	0.09	0.03	45	0	14.60	79.28	512.41	20.90
44	160	800	0.09	0.03	45	0	19.87	68.65	366.55	13.09
45	140	800	0.07	0.03	45	90	4.71	88.49	327.83	8.79
46	160	800	0.07	0.03	45	90	4.76	89.06	386.66	19.23
47	140	800	0.09	0.03	45	90	4.21	85.47	266.28	2.62
48	160	800	0.09	0.03	45	90	5.59	72.59	386.67	8.83
49	150	800	0.08	0.03	45	45	9.33	89.24	181.02	8.29
50	150	800	0.08	0.03	45	45	8.87	86.38	246.68	6.62
51	150	800	0.08	0.03	45	45	10.52	79.02	195.18	6.57
52	150	800	0.08	0.03	45	45	12.64	81.20	191.50	1.59
53	150	800	0.08	0.03	45	45	10.33	82.59	152.35	3.19
54	150	800	0.08	0.03	45	45	8.95	85.10	194.44	1.69

Figure 5. As shown in Figure 5, the actual values are basically distributed on the predicted curves and the actual values are consistent with the trend of the predicted values, showing

linear distribution. In general, the models verify the experimental data accurately, so the models can predict and analyze the effect of various factors on the indexes.

TABLE 4: Analysis of variance of surface roughness.

Source	Sum of squares	DF	Mean square	F value	p value prob > F
Model	1172.94	27	43.44	10.47	<0.0001
A	1.71	1	1.71	0.41	0.5263
B	1.153×10^{-3}	1	1.153×10^{-3}	2.778×10^{-4}	0.9868
C	2.044×10^{-3}	1	2.044×10^{-3}	4.927×10^{-4}	0.9825
D	119.63	1	119.63	28.83	<0.0001
E	4.67	1	4.67	1.13	0.2983
F	767.11	1	767.11	184.88	<0.0001
AB	1.02	1	1.02	0.24	0.6248
AC	17.07	1	17.07	4.11	0.0529
AD	0.13	1	0.13	0.031	0.8620
AE	0.11	1	0.11	0.027	0.8698
AF	0.19	1	0.19	0.045	0.8331
BC	2.00	1	2.00	0.48	0.4934
BD	0.53	1	0.53	0.13	0.7236
BE	3.59	1	3.59	0.86	0.3610
BF	0.49	1	0.49	0.12	0.7334
CD	7.34	1	7.34	1.77	0.1949
CE	0.84	1	0.84	0.20	0.6556
CF	1.12	1	1.12	0.27	0.6076
DE	0.22	1	0.22	0.052	0.8217
DF	91.57	1	91.57	22.07	<0.0001
EF	16.06	1	16.06	3.87	0.0599
Residual	107.88	26	4.15		
Lack of fit	97.78	21	4.66	2.31	0.1801
Pure error	10.10	5	2.02		
Cor total	1280.82	53			

TABLE 5: Analysis of variance of density.

Source	Sum of squares	DF	Mean square	F value	p value prob > F
Model	2035.96	27	75.41	8.30	<0.0001
A	9.45	1	9.45	1.04	0.3171
B	77.01	1	77.01	8.48	0.0073
C	284.59	1	284.59	31.33	<0.0001
D	617.80	1	617.80	68.01	<0.0001
E	5.29	1	5.29	0.58	0.4524
F	193.92	1	193.92	21.35	<0.0001
AB	2.46	1	2.46	0.27	0.6071
AC	124.75	1	124.75	13.73	0.0010
AD	36.18	1	36.18	3.98	0.0565
AE	9.62	1	9.62	1.06	0.3130
AF	10.56	1	10.56	1.16	0.2907
BC	22.97	1	22.97	2.53	0.1239
BD	75.91	1	75.91	8.36	0.0077
BE	10.67	1	10.67	1.17	0.2884
BF	8.24	1	8.24	0.91	0.3497
CD	40.77	1	40.77	4.49	0.0438
CE	1.84	1	1.84	0.20	0.6560
CF	1.00	1	1.00	0.11	0.7425
DE	166.10	1	166.10	18.29	0.0002
DF	73.58	1	73.58	8.10	0.0085
EF	56.59	1	56.59	6.23	0.0192
Residual	236.18	26	9.08		
Lack of fit	167.32	21	7.97	0.58	0.8281
Pure error	68.86	5	13.77		
Cor total	2272.13	53			

TABLE 6: Analysis of variance of tensile strength.

Source	Sum of squares	DF	Mean square	F value	p value prob > F
Model	1.227×10^6	27	45454.48	14.31	<0.0001
A	30861.77	1	30861.77	9.72	0.0044
B	44371.38	1	44371.38	13.97	0.0009
C	8444.14	1	8444.14	2.66	0.1150
D	6.023×10^5	1	6.023×10^5	189.67	<0.0001
E	686.54	1	686.54	0.22	0.6458
F	50015.45	1	50015.45	15.75	0.0005
AB	0.16	1	0.16	4.947×10^{-5}	0.9944
AC	4936.40	1	4936.40	1.55	0.2236
AD	25955.86	1	25955.86	8.17	0.0083
AE	3.46	1	3.46	1.089×10^{-3}	0.9739
AF	5545.85	1	5545.85	1.75	0.1978
BC	2596.73	1	2596.73	0.82	0.3741
BD	22248.05	1	22248.05	7.01	0.0136
BE	5530.04	1	5530.04	1.74	0.1985
BF	7718.38	1	7718.38	2.43	0.1311
CD	577.70	1	577.70	0.18	0.6732
CE	686.80	1	686.80	0.22	0.6458
CF	594.23	1	594.23	0.19	0.6689
DE	2029.53	1	2029.53	0.64	0.4313
DF	113.57	1	113.57	0.036	0.8515
EF	11412.79	1	11412.79	3.59	0.0692
Residual	82562.08	26	3175.46		
Lack of fit	77877.06	21	3708.43	3.96	0.0663
Pure error	4685.02	5	937.00		
Cor total	1.310×10^6	53			

TABLE 7: Analysis of variance of elongation.

Source	Sum of squares	DF	Mean square	F value	p value prob > F
Model	10386.66	27	384.69	14.05	<0.0001
A	350.33	1	350.33	12.80	0.0014
B	138.03	1	138.03	5.04	0.0335
C	89.58	1	89.58	3.27	0.0820
D	4864.16	1	4864.16	177.70	<0.0001
E	1.30	1	1.30	0.048	0.8289
F	58.73	1	58.73	2.15	0.1550
AB	333.82	1	333.82	12.20	0.0017
AC	34.91	1	34.91	1.28	0.2691
AD	51.06	1	51.06	1.87	0.1837
AE	336.05	1	336.05	12.28	0.0017
AF	49.00	1	49.00	1.79	0.1925
BC	0.076	1	0.076	2.762×10^{-3}	0.9585
BD	195.25	1	195.25	7.13	0.0129
BE	39.24	1	39.24	1.43	0.2420
BF	4.86	1	4.86	0.18	0.6771
CD	3.90	1	3.90	0.14	0.7087
CE	1.58	1	1.58	0.058	0.8120
CF	0.16	1	0.16	5.684×10^{-3}	0.9405
DE	107.43	1	107.43	3.92	0.0582
DF	325.69	1	325.69	11.90	0.0019
EF	14.25	1	14.25	0.52	0.4770
Residual	711.70	26	27.37		
Lack of fit	670.62	21	31.93	3.89	0.0687
Pure error	41.08	5	8.22		
Cor total	11098.36	53			

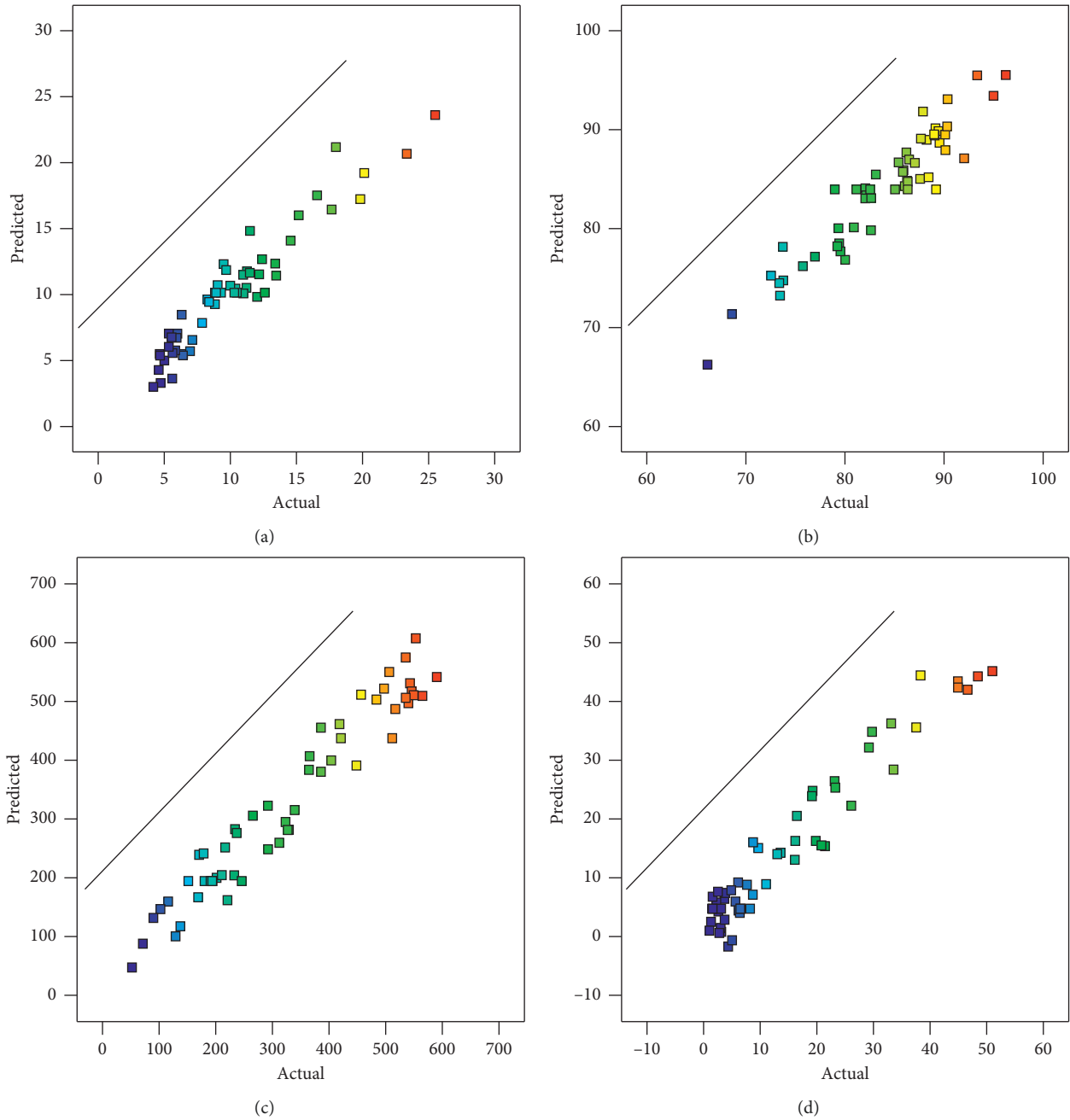


FIGURE 5: Scatter plot: predicted values of (a) surface roughness, (b) density, (c) tensile strength, and (d) elongation.

Within the horizontal range of the selected factors, the weight of effect on the surface roughness according to the F value of each factor is the angle with the xy plane > layer thickness > the angle with the xz plane > laser power > hatching space > scan speed; the weight of effect on the density is layer thickness > hatching space > the angle with the xy plane > scan speed > laser power > the angle with the xz plane; the weight of effect on tensile strength is layer thickness > the angle with the xy plane > scan speed > laser power > hatching space > the angle with the xz plane; and the weight of effect on elongation is layer thickness > laser

power > scan speed > hatching space > the angle with the xy plane > the angle with the xz plane.

3.1.2. *Analysis of Multivariate Interactive Influence.* When laser power, scan speed, hatching space, and the angle with the xz plane are constant, it can be seen from Figure 6 that when the angle with the xy plane is 0° , the surface roughness increases as the layer thickness increases, reaches the peak as the layer thickness further increases, and then decreases as the layer thickness continues to

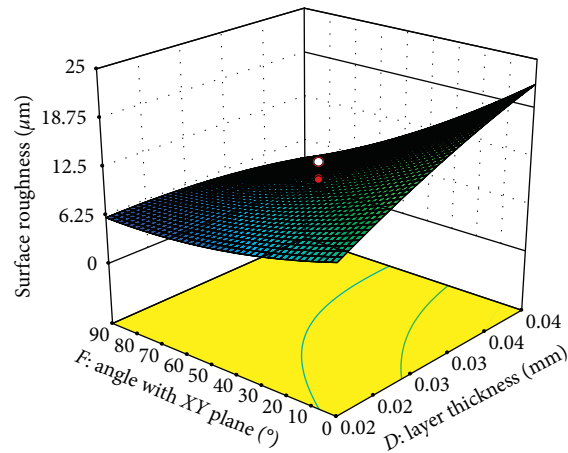


FIGURE 6: Effect of layer thickness and the angle with the xy plane on surface roughness.

increase; when the layer thickness is constant, the surface roughness decreases as the angle with the xy plane increases.

As shown in Figure 7(a), when both laser power and scan speed increase, the density first increases and then decreases. When the laser power is 160 W and the hatching space is 0.07 mm, the density reaches the peak; when the hatching space ranges from 0.07 to 0.08 mm, the density increases as the laser power increases; and when the hatching space ranges from 0.08 to 0.09 mm, the density decreases as the laser power increases. As shown in Figure 7(b), when the layer thickness is constant, the density decreases as the scan speed increases; and when the scan speed is constant, the density increases as the layer thickness increases. As shown in Figure 7(c), when the layer thickness is 0.02 mm, the density increases first and then decreases as the hatching space increases; and when the scan speed is 0.09 mm/s, the density decreases at the fastest rate as the layer thickness increases. As shown in Figure 7(d), when the angle with the xy plane is constant, the density decreases as the layer thickness increases; when the angle with the xy plane is 0° , the density decreases at the fastest rate; when the layer thickness is constant, the density increases as the angle with the xy plane increases, and when the layer thickness is 0.04 mm, the density increases at the fastest rate as the angle with the xy plane increases. As shown in Figure 7(e), when the layer thickness is 0.02 mm, the density increases as the angle with the xz plane increases, reaching the maximum value, but the trend of density changes as the layer thickness further increases, and when layer thickness is above 0.02 mm, the density decreases as the angle with the xz plane increases. As shown in Figure 7(f), when the angle with the xy plane ranges from 0° to 50° , the density decreases as the angle with the xz plane increases, and when the angle with the xy plane ranges from 50° to 90° , the density increases as the angle with the xz plane increases.

As shown in Figure 8(a), when the laser power is constant, the tensile strength decreases as the layer thickness increases; when the laser power is 140 W, the tensile strength decreases at the fastest rate; when the laser power is 160 W, the tensile strength decreases at the slowest rate; and when the layer

thickness is constant, the tensile strength increases as the laser power increases. As shown in Figure 8(b), when the layer thickness is constant, the tensile strength decreases as the scan speed increases; when the layer thickness is 0.04 mm, the tensile strength decreases at the fastest rate; when the scan speed is constant, the tensile strength decreases as the layer thickness increases; and when the scan speed is 900 mm/s, the tensile strength decreases at the fastest rate.

As shown in Figure 9(a), when the scan speed ranges from 700 to 760 mm/s, the elongation increases as the laser power increases; when the scan speed ranges from 760 to 900 mm/s, the elongation first decreases and then increases as the laser power increases; when the laser power ranges from 140 to 148 W, the elongation increases as the scan speed increases; when the laser power ranges from 148 to 160 W, the elongation decreases first and then increases as the scan speed increases; and at the minimum scan speed and the maximum laser power, the elongation reaches the maximum value. As shown in Figure 9(b), when the angle with the xz plane ranges from 0° to 50° , the elongation decreases first and then increases as the laser power increases; when the angle with the xz plane ranges from 50° to 90° , the elongation increases as the laser power increases; when the laser power ranges from 140 to 150 W, the elongation decreases as the angle with the xz plane increases; and when the laser power ranges from 150 to 160 W, the elongation increases as the angle with xz plane increases, reaching the maximum value together with the angle with the xz plane, laser power, and elongation. As shown in Figure 9(c), when the scan speed ranges from 700 to 800 mm/s, the elongation decreases first and then increases as the layer thickness increases; when the scan speed ranges from 800 to 900 mm/s, the elongation decreases as the layer thickness increases; when the layer thickness ranges from 0.02 to 0.03 mm, the elongation does not change significantly as the scan speed increases; and when the layer thickness ranges from 0.03 to 0.04 mm, the elongation decreases as the scan speed increases, and the maximum elongation is obtained from the minimum layer thickness and maximum scan speed. As shown in Figure 9(d), when the angle with the xy plane is constant, the elongation decreases rapidly first and then increases slowly as the layer thickness increases; when the layer

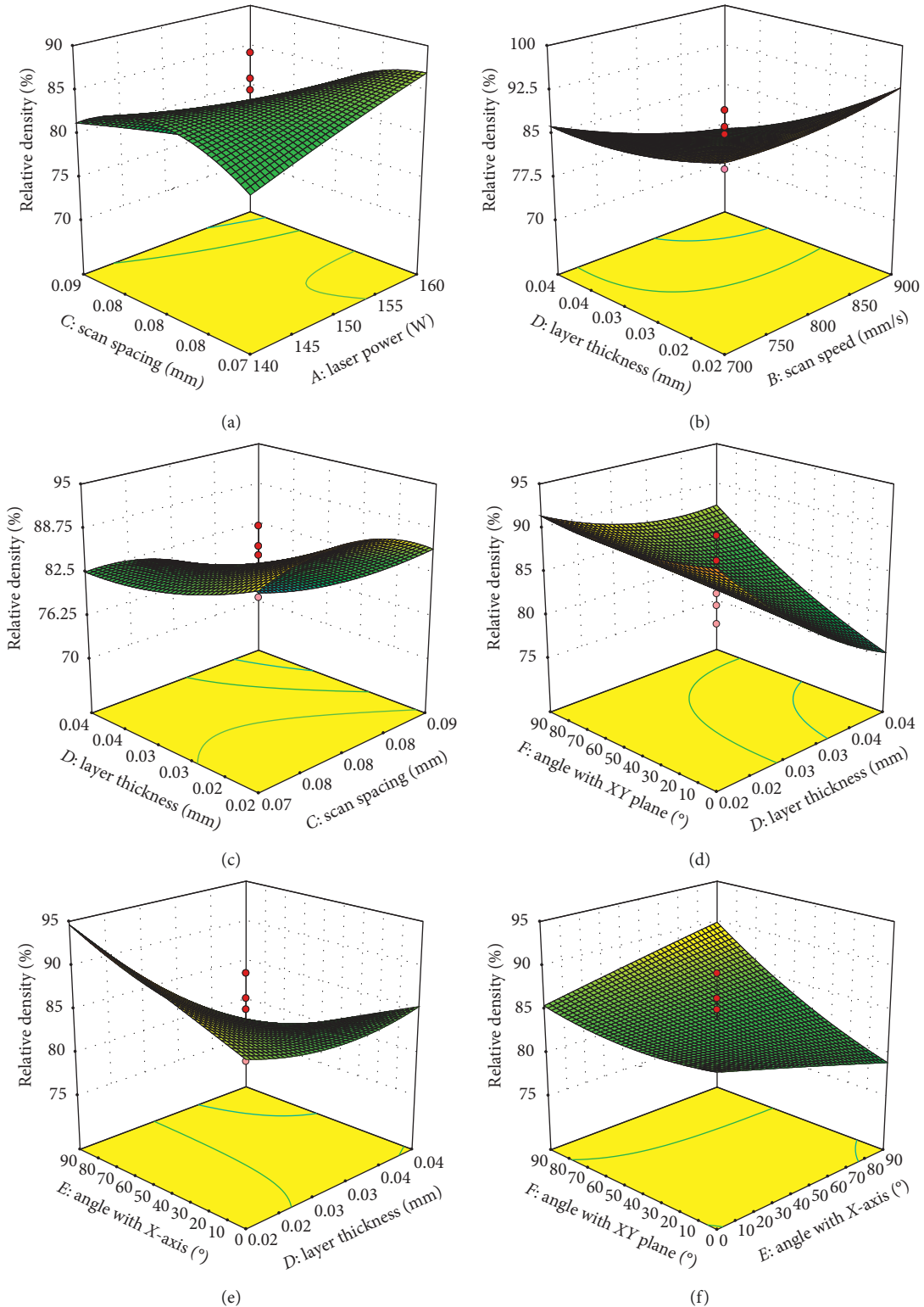


FIGURE 7: Effect of laser power, scan speed, scan spacing, layer thickness, angle with the xz plane, and angle with the xy plane on density. (a) Effect of interaction of laser power and scan spacing on density. (b) Effect of interaction of scan speed and layer thickness on density. (c) Effect of interaction of scan spacing and layer thickness on density. (d) Effect of interaction of angle with the xy plane and layer thickness on density. (e) Effect of interaction of angle with the xz plane and layer thickness on density. (f) Effect of interaction of angle with the xy plane and angle with the xz plane on density.

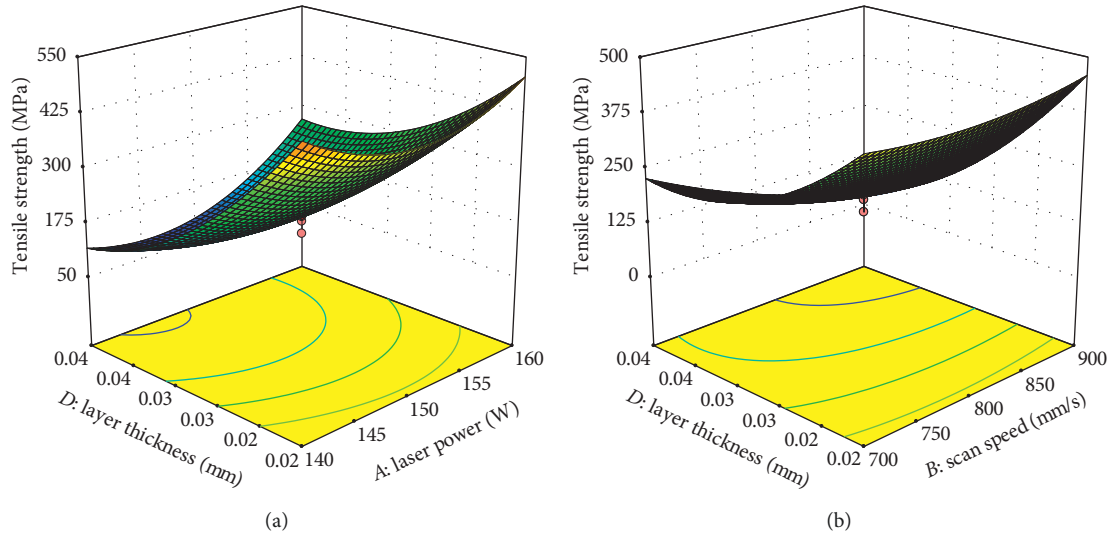


FIGURE 8: Effect of laser power, scan speed, and layer thickness on tensile strength. (a) Effect of interaction of laser power and layer thickness on tensile strength. (b) Effect of interaction of scan speed and layer thickness on tensile strength.

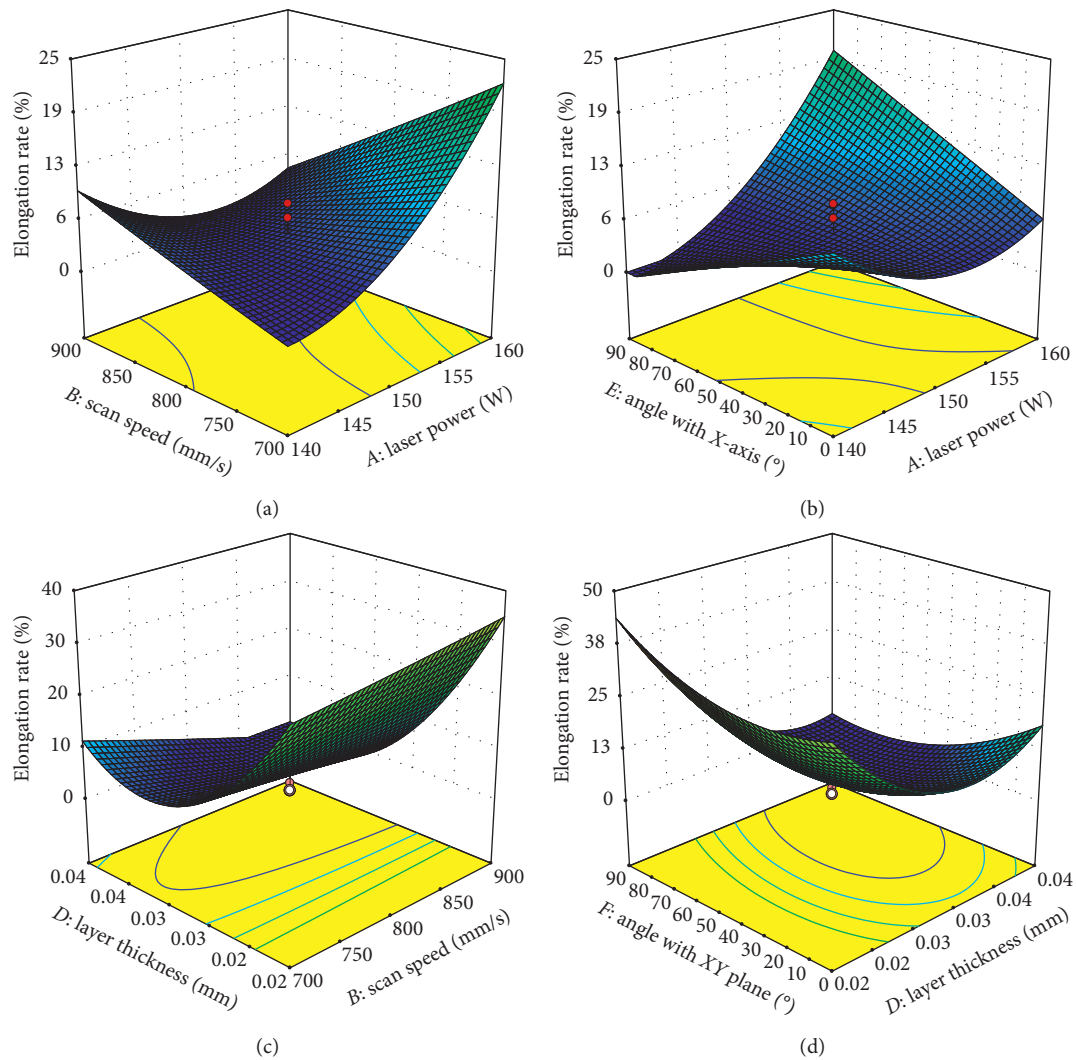


FIGURE 9: Effect of laser power, scan speed, scan spacing, layer thickness, angle with xz plane, and angle with xy plane on elongation. (a) Effect of interaction of scan speed and laser power on elongation. (b) Effect of interaction of angle with the xz plane and laser power on elongation. (c) Effect of interaction of scan speed and layer thickness on elongation. (d) Effect of interaction of angle with the xy plane and layer thickness on elongation.

thickness ranges from 0.02 to 0.023 mm, the elongation increases as the angle with the xy plane increases; and when the layer thickness ranges from 0.024 to 0.04 mm, the elongation decreases first and then increases as the angle with the xy plane increases.

3.1.3. Optimization of Process Parameters. Based on the above experiments, the predicted and actual optimization results are shown in Table 8 and formula (8). The error between the predicted and actual values of the surface roughness under optimized conditions is 4.6%, the error between the predicted and actual values of the density is 1%, the error between the predicted and actual values of the tensile strength is 19.5%, and the error between the predicted and actual values of the elongation is 18.9%. All errors are within the reasonable range, indicating that the results are reliable. The tensile strength and elongation of the formed parts with the optimal parameters are higher than that specified in ASTM-A182 and ASTM-F3184-16.

$$\left\{ \begin{array}{l} 140 \leq A \leq 160, \\ 700 \leq B \leq 900, \\ 0.07 \leq C \leq 0.09, \\ 0.02 \leq D \leq 0.04, \\ 0 \leq E \leq 90, \\ 0 \leq F \leq 9, \\ \gamma_1 = f_1(A, B, C, D, E, F), \\ \min Y_1, \\ \max Y_2, \\ \max Y_3, \\ \max Y_4. \end{array} \right. \quad (8)$$

3.2. Microstructure and Fracture Morphology Analysis

3.2.1. Microstructure Analysis. As shown in Figure 10(a), the microstructure of the selective laser melting sample before stretching is mainly composed of a plurality of oval molten pools, each of which has an aspect ratio of 0.5–0.65. This study suggests that there is certain unevenness in the powder size, a difference in laser energy absorption, and a Gaussian distribution of laser energy, which helps shape the oval molten pools due to different energy densities in various areas. Figure 10(b) shows the shape of the molten pools after stretching. Compared with Figure 10(a), the molten pools of the parts are obviously elongated after stretching with an aspect ratio of 2–1.5, or 2–4 times of that before stretching. Figures 10(c) and 10(d) show the microstructure before stretching. It can be seen from Figures 10(c) and 10(d) that the inside of the molten pool is mainly composed of equiaxed crystals and columnar crystals. The grain sizes are fine with a width of 0.28–0.4 nm, of which, the secondary arm of the columnar crystal is not developed and the morphology of the dendrites is not significant, with obvious

planar crystals at the junction of the layers. The columnar crystals in the microstructure show apparent epitaxial growth characteristics because the laser melting process is at a high temperature gradient and solidification rate, while forming material and substrate temperature are lower, generally lower than the forming temperature by several orders of magnitude, resulting in heat transfer from the processing layer to the formed layer from top to bottom. The solidification direction inside the molten pool is from the bottom to the top of the molten pool, with solidification conditions in the growth range of equiaxed crystals and columnar crystals. Due to the rapid condensation of the laser, the bottom of the molten pool is closest to the formed layer with fastest solidification. The crystal grains at the bottom of the molten pool are solidified without growing, so equiaxed crystals appear at the bottom and boundary of the molten pool in the form of relatively fine grains, showing a planar crystal with white and bright layers of microstructure.

3.2.2. Hardness Analysis. The microhardness of the experiment is shown in Figure 11. The distance closest to the fracture is set as 0, and three points are selected at each distance to obtain the average. As shown in Figure 11, the microhardness of the sample increases first and then decreases with the increase in the distance. The average microhardness at 2.5 mm from the fracture is 28.73 HRC, and the average microhardness at 20 mm from the fracture is 25.23 HRC, which is 87% of the hardness at the fracture. The microhardness at the fracture is significantly higher than the substrate because the fracture has a large number of dislocations, and dislocation multiplication and increased surface energy help improve the hardness.

3.2.3. XRD Analysis. The XRD of the sample formed by optimizing the parameters is shown in Figure 12. Compared with the standard map, the diffraction peak intensity of the crystal planes increases at γ -Fe (111), and the diffraction peak intensity of the crystal planes decreases at γ -Fe (200) and γ -Fe (220), showing that the γ -Fe crystallinity is not as good as the standard map. When the diffraction angle ranges from 40° to 45° , a significant diffraction peak broadening occurs. The diffraction peak broadening is determined by two physical factors, grain refinement and crystal microscopic distortion.

3.2.4. Fracture Analysis. The fracture morphology is shown in Figure 13. As shown in Figure 13(a), there are a large number of clear dimples whose shapes have obvious tearing, called elongated dimples, and the specimen fracture is a typical plastic fracture. Figure 13(b) shows fracture cracks passing through the grains, which is known as a transgranular fracture, and there are many dimples in the fracture, which is a ductile fracture. The specimen fracture is mainly caused by a large amount of dislocation multiplication under tensile stress with increased grain boundary energy, and a great quantity of impurities in the

TABLE 8: Predicted and actual results under optimized conditions.

Exp. no.	Laser power (W)	Scanning speed (mm/s)	Scanning interval (mm)	Layer thickness (mm)	Angle with the xz plane	Angle with the xy plane	Surface roughness (μm)	Relative density (%)	Tensile strength (MPa)	Elongation rate (%)
Predicted values	160	836	0.07	0.02	83.3	89.7	4.1	97.27	609.5	55.9
Actual value	160	836	0.07	0.02	83.3	89.7	4.3	96.3	510	47
Relative error							4.6%	1%	19.5%	18.9%

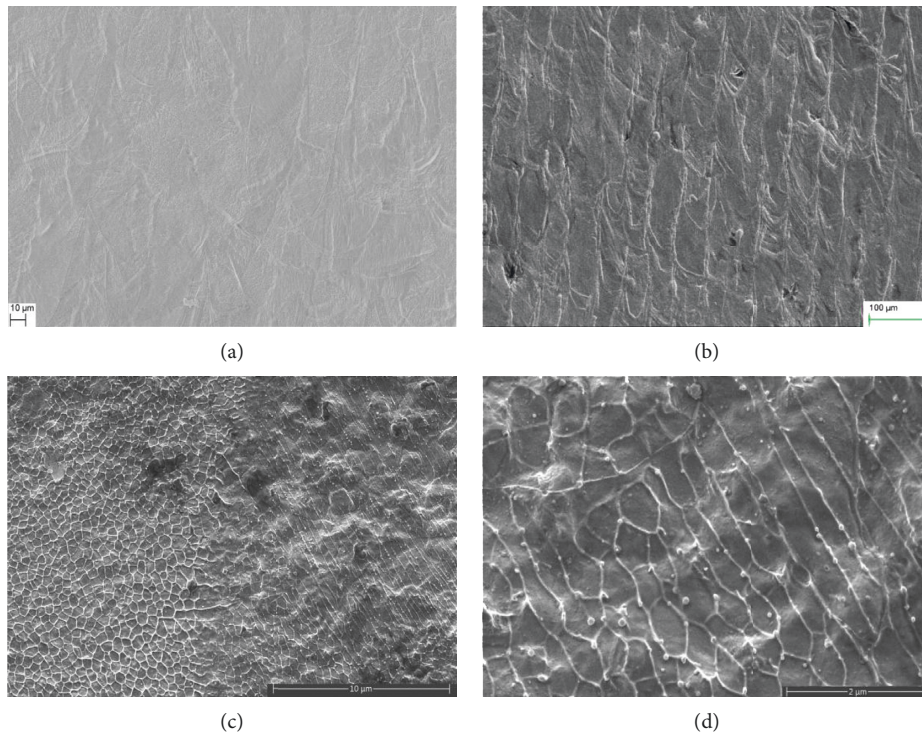


FIGURE 10: Microstructure. (a) Molten pool before stretching. (b) Molten pool after stretching. (c) Microstructure in molten pool. (d) Partial enlargement of microstructure in molten pool.

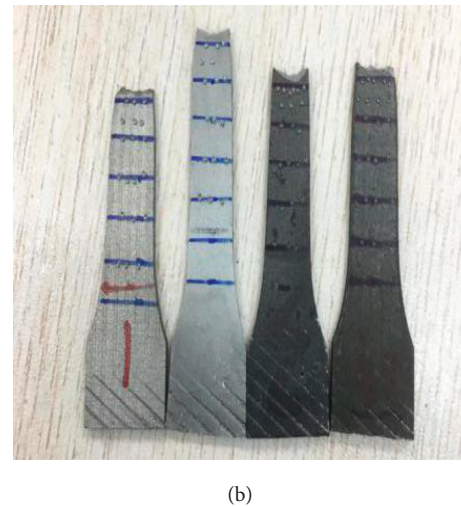
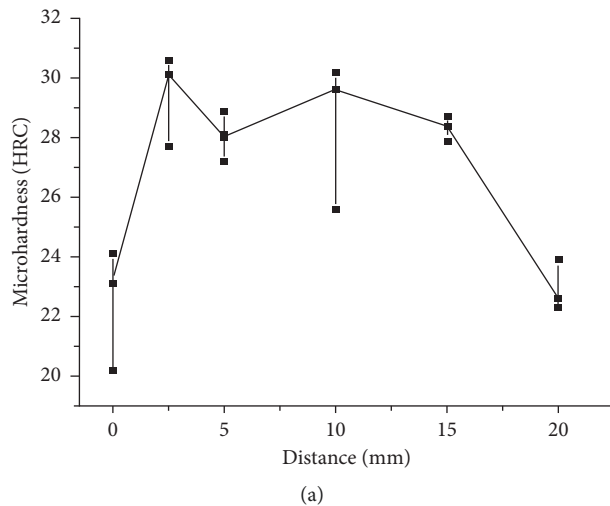


FIGURE 11: Microhardness. (a) Hardness curve. (b) Hardness physical image.

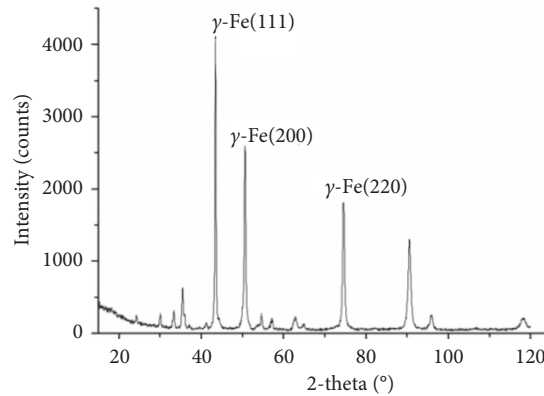


FIGURE 12: XRD.

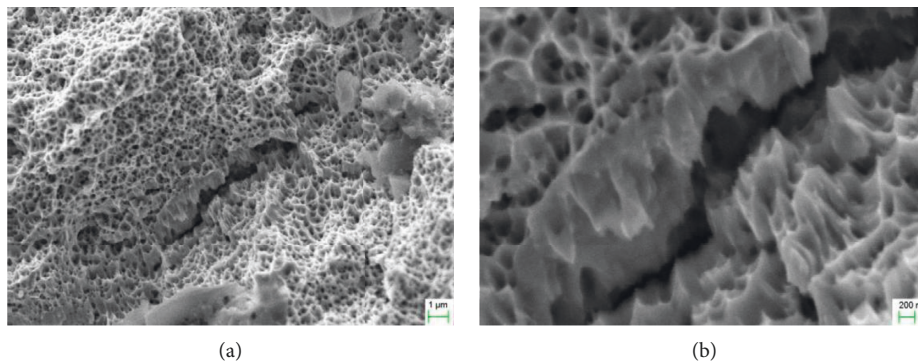


FIGURE 13: Fracture morphology. (a) Dimple morphology. (b) Crack.

material are broken to form a plenty of micropores. The micropores further grow under external force to generate cracks until the final failure.

4. Conclusion

- (1) The angle with the xz plane has a significant effect on the experiment indexes. The comprehensive factor that has the greatest effect on the experiment indexes is the layer thickness. The biggest effect on the surface roughness is from the angle with the xy plane.
- (2) The optimal forming parameters are laser power of 160 W, scan speed of 836 mm/s, hatching space of 0.07 mm, layer thickness of 0.02 mm, the angle with the xz plane of 83.3° , and the angle with the xy plane of 89.7° . The errors between the predicted values and the actual values of the surface roughness, the density, the tensile strength, and the elongation under optimized conditions are 4.6%, 1%, 19.5%, and 18.9%, respectively, and the errors are within a reasonable range, indicating that the model has practical engineering value.
- (3) After stretching, the molten pools of the parts are obviously elongated with the aspect ratio increasing from 0.5–0.65 to 1.5–2, up by 130%–300%. The microstructure of the formed parts is composed of equiaxed crystals and columnar crystals with a grain

width of 0.28–0.4 nm. The secondary growth of dendrites is not obvious, with the microstructure showing directional solidification. XRD analysis shows that the crystallinity of the selective laser melting parts is not as good as that of the standard sample, with grain refinement and microscopic distortion of crystals.

- (4) There are many dimples in the fracture which is ductile fracture and typical plastic fractures, and the hardness near the fracture is greatly higher, or 1.14 times that of the substrate. The indexes regarding the selective laser melting parts are better than the ASTM-A182 and ASTM-F3184-16 standards.

Data Availability

The figure and table data used to support the findings of this study are available from the corresponding author upon request.

Conflicts of Interest

The authors declare that they have no conflicts of interest.

Acknowledgments

This research was supported by the China Agriculture Research System (CARS-31), the Guangzhou Science and

Technology Plan Project (no. 201710010105), and the National Natural Science Foundation of Guangdong Province (no. 2019A1515011039). The authors wish to thank their generous financial assistance.

References

- [1] H. Li, M. Ramezani, M. Li, C. Ma, and J. Wang, "Tribological performance of selective laser melted 316L stainless steel," *Tribology International*, vol. 128, pp. 121–129, 2018.
- [2] P. Hanzl, M. Zetek, T. Bakša, and T. Kroupa, "The influence of processing parameters on the mechanical properties of SLM parts," *Procedia Engineering*, vol. 100, pp. 1405–1413, 2015.
- [3] S. Yusuf, Y. Chen, R. Boardman, S. Yang, and N. Gao, "Investigation on porosity and microhardness of 316L stainless steel fabricated by selective laser melting," *Metals*, vol. 7, no. 2, p. 64, 2017.
- [4] L. Yang, Z. Jian, and P. Zhicong, "Numerical and experimental investigation into the subsequent thermal cycling during selective laser melting of multi-layer 316L stainless steel," *Optics and Laser Technology*, vol. 98, pp. 23–32, 2018.
- [5] Z. Zheng, L. Wang, and B. Yan, "Effects of laser power on the microstructure and mechanical properties of 316L stainless steel prepared by selective laser melting," *International Journal of Modern Physics B*, vol. 31, no. 16–19, p. 1744015, 2017.
- [6] Z. Sun, X. Tan, S. B. Tor, and W. Y. Yeong, "Selective laser melting of stainless steel 316L with low porosity and high build rates," *Materials & Design*, vol. 104, pp. 197–204, 2016.
- [7] S. Tsopanos, R. A. W. Mines, S. McKown et al., "The influence of processing parameters on the mechanical properties of selectively laser melted stainless steel microlattice structures," *Journal of Manufacturing Science and Engineering*, vol. 132, no. 4, pp. 105–115, 2010.
- [8] M. Wei, S. Chen, L. Xi, J. Liang, and C. Liu, "Selective laser melting of 24CrNiMo steel for brake disc: fabrication efficiency, microstructure evolution, and properties," *Optics & Laser Technology*, vol. 107, pp. 99–109, 2018.
- [9] J. Delgado, J. Ciurana, and C. A. Rodríguez, "Influence of process parameters on part quality and mechanical properties for DMLS and SLM with iron-based materials," *The International Journal of Advanced Manufacturing Technology*, vol. 60, no. 5–8, pp. 601–610, 2012.
- [10] H. Li, M. Ramezani, M. Li, C. Ma, and J. Wang, "Effect of process parameters on tribological performance of 316L stainless steel parts fabricated by selective laser melting," *Manufacturing Letters*, vol. 16, pp. 36–39, 2018.
- [11] E. Liverani, S. Toschi, L. Ceschini, and A. Fortunato, "Effect of selective laser melting (SLM) process parameters on microstructure and mechanical properties of 316L austenitic stainless steel," *Journal of Materials Processing Technology*, vol. 249, pp. 255–263, 2017.
- [12] D. Wang, S. Wu, Y. Yang et al., "The effect of a scanning strategy on the residual stress of 316L steel parts fabricated by selective laser melting (SLM)," *Materials*, vol. 11, no. 10, p. 1821, 2018.
- [13] J. J. S. Dilip, G. D. J. Ram, T. L. Starr, and B. Stucker, "Selective laser melting of HY100 steel: process parameters, microstructure and mechanical properties," *Additive Manufacturing*, vol. 13, pp. 49–60, 2017.
- [14] K. N. Amato, S. M. Gaytan, L. E. Murr et al., "Microstructures and mechanical behavior of Inconel 718 fabricated by selective laser melting," *Acta Materialia*, vol. 60, no. 5, pp. 2229–2239, 2012.
- [15] Q. Wei, S. Li, C. Han et al., "Selective laser melting of stainless-steel/nano-hydroxyapatite composites for medical applications: microstructure, element distribution, crack and mechanical properties," *Journal of Materials Processing Technology*, vol. 222, pp. 444–453, 2015.
- [16] E. Brandl, U. Heckenberger, V. Holzinger, and D. Buchbinder, "Additive manufactured AlSi10Mg samples using Selective Laser Melting (SLM): microstructure, high cycle fatigue, and fracture behavior," *Materials & Design*, vol. 34, pp. 159–169, 2012.
- [17] X. F. Jiang, Z. Y. Xiong, H. T. Wang, H. J. Zhang, and Y. F. Wang, "Investigation on the mechanical properties of 316L metal powders by SLM," *Journal of Zhejiang University of technology*, vol. 45, pp. 510–515, 2017.
- [18] A. Yadollahi, N. Shamsaei, S. M. Thompson, and D. W. Seely, "Effects of process time interval and heat treatment on the mechanical and microstructural properties of direct laser deposited 316L stainless steel," *Materials Science and Engineering: A*, vol. 644, pp. 171–183, 2015.
- [19] A. B. Spierings, M. Schoepf, R. Kiesel, and K. Wegener, "Optimization of SLM productivity by aligning 17-4PH material properties on part requirements," *Rapid Prototyping Journal*, vol. 20, no. 6, pp. 444–448, 2014.
- [20] K. Parthiban, M. Duraiselvam, and R. Manivannan, "TOPSIS based parametric optimization of laser micro-drilling of TBC coated nickel based superalloy," *Optics & Laser Technology*, vol. 102, pp. 32–39, 2018.
- [21] R. Casati, J. Lemke, and M. Vedani, "Microstructure and fracture behavior of 316L austenitic stainless steel produced by selective laser melting," *Journal of Materials Science & Technology*, vol. 32, no. 8, pp. 738–744, 2016.
- [22] D. Wang, C. Song, Y. Yang, and Y. Bai, "Investigation of crystal growth mechanism during selective laser melting and mechanical property characterization of 316L stainless steel parts," *Materials & Design*, vol. 100, pp. 291–299, 2016.
- [23] A. Riemer, S. Leuders, M. Thöne, H. A. Richard, T. Tröster, and T. Niendorf, "On the fatigue crack growth behavior in 316L stainless steel manufactured by selective laser melting," *Engineering Fracture Mechanics*, vol. 120, pp. 15–25, 2014.
- [24] G. Miranda, S. Faria, F. Bartolomeu et al., "Predictive models for physical and mechanical properties of 316L stainless steel produced by selective laser melting," *Materials Science and Engineering: A*, vol. 657, pp. 43–56, 2016.
- [25] Y. Yin, P. Liu, C. Lu, M. Xiao, and R. Zhang, "Microstructure and tensile properties of selective laser melting forming 316L stainless steel," *Transactions of the China Welding Institution*, vol. 39, pp. 77–81, 2018.
- [26] J. A. Cherry, H. M. Davies, S. Mehmood, N. P. Lavery, S. G. R. Brown, and J. Sienz, "Investigation into the effect of process parameters on microstructural and physical properties of 316L stainless steel parts by selective laser melting," *The International Journal of Advanced Manufacturing Technology*, vol. 76, no. 5–8, pp. 869–879, 2015.
- [27] J. Wang, L. Shen, Y. Yang, Y. Bi, and M. Wan, "Optimizing calibration of design points for non-road high pressure common rail diesel engine base on response surface methodology," *Transactions of the Chinese Society of Agricultural Engineering*, vol. 33, pp. 31–39, 2017.

